Geometrical and Chemical Dependent Hydrolysis Mechanisms of Silicon Nanomembranes for Biodegradable Electronics

Liu Wang[†♦], *Yuan Gao*[§♦], *Fanqi Dai*[†], *Deying Kong*[†], *Huachun Wang*[‡], *Pengcheng Sun*[†], *Zhao Shi*[‡], *Xing Sheng*[‡], *Baoxing Xu*[*§], *Lan Yin*[*†]

[†]School of Materials Science and Engineering, The Key Laboratory of Advanced Materials of Ministry of Education, State Key Laboratory of New Ceramics and Fine Processing, Tsinghua University, Beijing 100084, P. R. China

[‡]Department of Electronic Engineering, Beijing National Research Center for Information Science and Technology, and Beijing Innovation Center for Future Chips, Tsinghua University, Beijing 100084, P. R. China

[§]Department of Mechanical and Aerospace Engineering, University of Virginia, Charlottesville, Virginia 22904, United States

Keywords: biodegradable electronics, silicon dissolution, size-dependent hydrolysis, surface-charge status, silicon/solution interface

Abstract

Biodegradable electronic devices that physically disappear in physiological or environmental solutions are of critical importance for widespread applications in healthcare management and environmental sustainability. The precise modulation of materials and device dissolution with on-demand operational lifetime, however, remain a key challenge. Silicon nanomembranes (Si NMs) are one of the essential semiconductor components for high-performance biodegradable electronics at system level. In this work, we discover unusual hydrolysis behaviors of Si NMs that are significantly dependent on the dimensions of devices as well as their surface chemistry status. The experiments show a pronounced increase in hydrolysis rates of p-type Si NMs with larger sizes and mechanical stirring introduces a significant decrease in dissolution rates. The presence of phosphates and potassium ions in solutions, or lower dopant levels of Si NMs will facilitate the degradation of Si NMs and will also lead to a stronger size-dependent effect. Molecular dynamics (MD) simulations are performed to reveal ion adsorption mechanisms of Si NMs under different surface charge status and confirm our experimental observations. Through geometrical designs, Si NMs based electrode arrays with tunable dissolution lifetime are formed and their electrochemical properties are analyzed *in vitro*. These results offer new controlling strategies to modulate the operational time frames of Si NMs through geometrical design and surface chemistry modification, and provide crucial fundamental understandings for engineering high-performance biodegradable electronics.

Introduction

Biodegradable electronics is an emerging class of technology whose key characteristic is that devices physically disappear in physiological or environmental solutions at controlled rates into harmless end products after the expecting operating period. [1] Devices with this property create application opportunities that lie outside of those of traditional electronic devices. Envisioned applications include temporary biomedical implants that avoid unnecessary device load without surgical intervention, "green" environmental monitors or sensors that eliminate the need for collection and recovery, and secure data storage systems that prevent unauthorized access of security information. [2-8] Constitute materials of biodegradable electronics such as semiconductors, dielectrics, and conductors should be biodegradable and biocompatible, and simultaneously provide desirable electrical properties. Demonstrated options include magnesium (Mg), iron (Fe), molybdenum (Mo), zinc (Zn), and tungsten (W) for the electrodes and interconnects; [9-12] magnesium oxide (MgO), silicon dioxide (SiO_2), silicon nitride (SiN_x), and spin-on-glass (SOG) for the dielectrics; [1, 13-14] polycaprolactone (PCL), polyglycolic acid (PGA), polylactic acid (PLA), polylactic-so-glycolic acid (PLGA) for the substrates and encapsulations; [15-16] and silicon (Si), germanium (Ge), zinc oxide (ZnO), and two-dimensional (2D) molybdenum disulfide (MoS_2) for the semiconductors. [17-21]

Considering the well-established scientific understanding and manufacturing infrastructure of silicon semiconductors, silicon nanomembranes (Si NMs) represent the essential active or passive components for high-performance biodegradable electronics at the system level, due to its excellent operational characteristics and hydrolysis in biofluids or groundwater over timescales

that are relevant for envisioned applications in biomedicine or green consumer electronics. Various devices based on Si NMs containing arrays of diodes, transistors, ring oscillators, and logic circuits have been demonstrated. [1] Bioresorbable electrocorticography (ECoG) Si neural electrodes and intracranial pressure and temperature Si sensors have been achieved and tested on animal models. [6-7] Si NMs have also been reported to serve as an excellent water barrier for passive neural recording arrays. [22] By leveraging the state-of-art silicon complementary metal oxide semiconductor (CMOS) foundries, various water-soluble integrated circuits can be achieved to establish the manufacturing routes for biodegradable implants, green consumer electronics, and unrecoverable systems. [23-25]

Detailed understanding of the mechanism of hydrolysis of Si NMs is therefore critical to design the working lifetime of the device. Previous studies of hydrolysis of Si have revealed that ion types and relevant concentrations, [26] temperatures, [2] pHs, [17] doping levels, [27] and the presence of proteins [22] can all strongly affect the dissolution rates of Si NMs. Systematic studies have shown that the dissolution rates of Si NMs with various doping levels cover a range of 0.01–398.11 nm/day in aqueous solutions with different pH values (2.6–8.2), ion concentrations, organic compounds (proteins), and temperatures. [2, 17, 22, 26] Higher concentrations of chlorides and phosphates, temperatures, and pH levels can greatly accelerate Si dissolution, while higher dopant concentrations ($>10^{20}$ cm^{-3}) dramatically decelerate the dissolution rates. [2, 17, 26] Additionally, calcium (Ca^{2+}) and magnesium (Mg^{2+}) ion concentrations can slightly increase the dissolution rates, while the presence of proteins slows down the dissolution. [22] The underlying mechanism studies suggest that Si dissolution proceeds through the nucleophilic attack of silicon surface bonds, which weakens the interior bonds and therefore assists in Si dissolution to form silicic acid

$Si(OH)_4$ as final biocompatible and environmentally benign end products. [26] Dissolution behavior of Si nanowire has also been studied and the coating of 10 nm thick Al_2O_3 can significantly extend its long-term stability. [21] Nevertheless, Si hydrolysis in aqueous solutions has been found to proceed in a non-uniform manner [22] and inconsistent dissolution rates have been reported with the same type of Si NM in the same type of aqueous solutions, suggesting more detailed investigation are needed so as to further understand the hydrolysis behavior and provide versatile methods to modulate the operational timeframes of degradable Si electronics.

Here, we present interesting size-dependent dissolution behavior of p-type Si NMs, in the sense that Si NMs with smaller size demonstrate slower dissolution rates, while introducing stirring slows down the dissolution rates significantly. On the contrary, no significant size-dependent behavior has been observed with n-type Si NMs. In order to reveal the underlying mechanism of these interesting counter-intuitive phenomenon, systematic studies have been performed to investigate the effects of the size of Si NMs on dissolution rates in various types of saline and buffer solutions with molar concentrations and pHs close to physiological conditions at 37 °C. The influence of stirring conditions as well as the concentrations and types of dopants have also been taken into account. It is hypothesized that the surface charge status of Si NMs plays an important role, and as a result influence the ion distributions at the Si/solution interface and modify the dissolution behavior. Molecular dynamics (MD) simulations are performed to understand the distribution of cations and anions at the Si/solution interface with different charge densities, and the ion absorption mechanism is revealed. Si electrodes with tunable lifetime based on p-type Si NMs have been achieved with different geometry design (pad or mesh type), demonstrating

alternative methods that can effectively modulate the operational timeframes of Si NMs to adapt various applications for biodegradable electronics.

Results and discussions

Figure 1a presents the schematic illustration of the test structure of Si hydrolysis. Experiments here involve measurements of the change in thickness as a function of soaking time of a patterned array of Si NMs squares (2000 × 2000 μm, 1000 × 1000 μm, 500 × 500 μm, 300 × 300 μm, 100 × 100 μm, 50 × 50 μm), derived from the top silicon layer of a silicon on insulator (SOI) wafer (Figure S1, S2, Supporting information). Figure 1b shows the representative thickness profiles measured by a profilometer at two stages of immersion (0 hour, left; 7 hours, right) in bicarbonate buffered solutions with pH 9.2 at 37 °C. Figure 1c summarizes the effects of size on the dissolution rates of Si NMs (p typed (boron), 10^{17} cm^{-3}, (100), 200 nm) in various types of saline buffered solutions with molar concentrations and pHs close to physiological conditions at 37 °C. In all cases, the rates of Si NMs show the size-dependent dissolution behavior and the dissolution rates enhance with increasing size of Si NMs. Besides, the dissolution rates of Si NMs in bicarbonate buffered solutions are the highest for all sizes, possibly due to the higher pH level, which is consistent with the previous report. [2]

In addition, the dissolution rates of Si NMs in sodium chloride solutions (NaCl, 100 mM) and sodium phosphate buffered solutions (Na_2HPO_4/NaH_2PO_4 10 mM) with pH 7.4 are studied in detail. Here, the molar concentration of the phosphate buffered solutions is the sum of Na_2HPO_4

and NaH_2PO_4 as conventionally used to describe buffer solutions. Phosphates (1 mM) were added to the NaCl solutions to maintain a constant pH level. Phosphate buffered solutions at pH 7.4 were prepared by sodium/potassium monobasic (NaH_2PO_4/KH_2PO_4) and dibasic (Na_2HPO_4/K_2HPO_4) (molar ratio 19/81). Although the concentration of phosphate solutions is 10 times lower than that of the chloride solutions, the dissolution rates of Si NMs with different sizes are relatively comparable, as shown in Figure 1c. The combination of NaCl (100 mM) with Na_2HPO_4/NaH_2PO_4 (10 mM) results in much higher dissolution rates of Si NMs, nearly 5 times of that in NaCl solutions (100 mM) and 5 times of that in Na_2HPO_4/NaH_2PO_4 solutions (10 mM).

For the same concentration of cations (Na^+), faster rates occur in phosphate solutions rather than chloride solutions, as shown in Figure 1d, suggesting a stronger accelerating effect of phosphates than that of chlorides as previously reported. [26] For the role of cation type (Na^+ and K^+), Figure 1e, f shows the difference in dissolution rates in solutions with the same concentration of anions (phosphates and chlorides). The results indicate that K^+ enhances the dissolution more effectively than Na^+ for all sizes of Si NMs, likely due to the difference of the frequency of solvent exchange between Na^+ and K^+, as will be discussed subsequently. Moreover, the enhanced dissolution effects in phosphate solutions is stronger than that in chloride solutions.

Figure 1g presents a representative optical image of a Si square (1000 × 1000 μm) captured after 4 hours of immersion in phosphate buffered solutions (Na_2HPO_4/NaH_2PO_4 10 mM). The color difference of different area indicates the spatially nonuniform hydrolysis behavior of Si NMs. The roughness (Rq) is measured by the atomic force microscopy (AFM, Bruker Multimode 8), which

is 5.01 nm for the pink area and 6.72 nm for the green area (34 % higher than that of the pink area), respectively. Figure S1e highlights the difference of color change and corresponding roughness for Si square (500 × 500 μm) after 4 hours of soaking in the same buffer solutions. Figure S1f shows the SEM image of the surface and edges of Si NMs (500× 500 μm) after soaking test in Na_2HPO_4/NaH_2PO_4 (10 mM) solution of 50 hours, this result combined with that of Figure 1b indicate that the dissolution on the edges is usually slower than that of the center area, which is probably because that the edge area is more sensitive to perturbation. Our thickness measurement is therefore performed mostly in the center area of the squares. When the square size gets smaller, the edge could have more influence to the measurement, but even for the smallest size of the Si NMs studied here, the area of the edges (200 nm × 50 μm for a 50 × 50 μm square) is much smaller than that of the top plane (50 × 50 μm), suggesting the influence of the edge area is probably much smaller compared to that of the center area.

A simplified empirical model is proposed to capture the experimentally observed trends of the size-dependent behavior. The model assumes a uniform dissolution behavior. The dissolution rates of Si NMs (R) could be written as Equation (1), where x is the size of Si NMs, b is the coefficient of size-dependent behavior, and r_0 is the pre-exponential factor. r_0 is associated with the concentrations of ions in the solutions and the activation energy of hydrolysis, e.g., r_0 for dissolution behavior in phosphate and chloride buffer solutions could be expressed as Equation (2), as reported in a previous model. [26] Here, k_0 is the Boltzmann constant, E_a is the activation energy for hydrolysis, $[H_2O]$ is the concentration of water and is approximately constant, and $[OH^-]$, $[PO_4^{3-}]$ and $[Cl^-]$ represent the concentration of each species respectively. k_0 is a constant

(Equation 3), with a value determined from previous studies of silicon etching at high pH (10–60 wt% KOH solutions, with pH between 13 and 14). [28]

$$R = r_0 (1\text{-}e^{-bx}) \quad (1)$$

$$r_0 = k_0 \exp(-E_a(PO_4^{3-})/k_BT) \exp(-E_a(Cl^-)/k_BT)[H_2O]^4[OH^-]^{0.25}[PO_4^{3-}]^{0.25}[Cl^-]^{0.25} \quad (2)$$

$$k_0 = 2480\ \mu m\ h\ r^{-1}\ (mol/L)^{-4.5} \quad (3)$$

The modeled size-dependent dissolution rates are shown as solid lines in Figure 1c-f. Based on the experimental data, the fitted pre-exponential factor (r_0), the coefficients of size-dependent behavior (b) and the degree of size-dependent dissolution rates of dR/dx are summarized in Table S1. For the same concentration of cations (Na^+), higher dR/dx occurs in phosphate solutions rather than chloride solutions, suggesting the size-dependent effect is stronger in phosphate solutions than that in chloride solutions. In addition, for the same concentration of cations (phosphates or chlorides), K^+ results in a higher value dR/dx than those of Na^+, indicating the stronger size-dependent effect in solutions containing K^+. Moreover, buffer solutions with higher concentrations of phosphates also demonstrate a stronger size-dependent behavior. The simplified empirical model can capture the basic trend of the size-dependent behavior, but there is a relatively large deviation between the fitted curves and the experimental results for certain samples. As the real dissolution generally proceeds in a non-uniform manner, which is not taken into account in the simplified model, the model can only capture the basic trend but not for the quantification of the size-dependent behavior. To further quantify the size-dependent behavior, a more complicated model is needed in the future to address the non-uniform dissolution behavior.

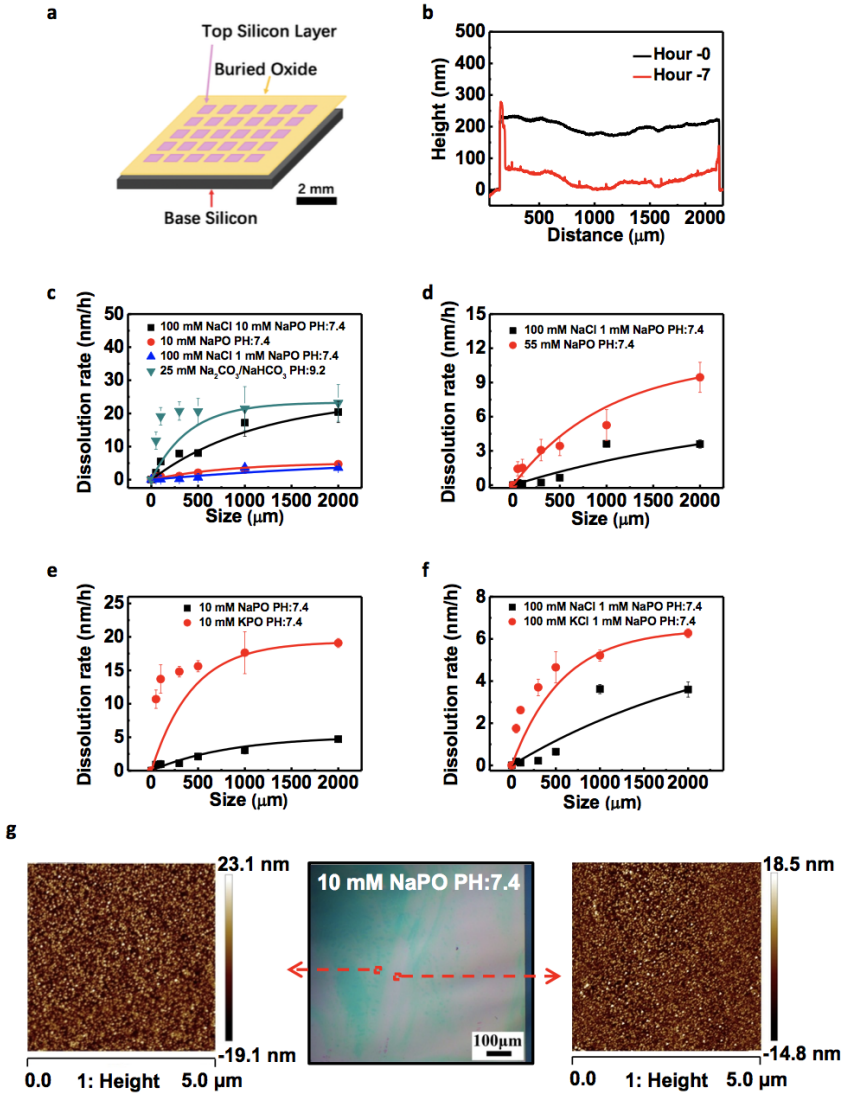

Figure 1. Hydrolysis of Si NMs in various types of saline buffered solutions with molar concentrations and pHs close to physiological condition at 37 °C. (a) Schematic illustration of the test structure, which consists of an array of Si squares , derived from the top silicon layer of a silicon on insulator (SOI) wafer; (b) Profiles of Si pads (2000 × 2000 μm) at different stages of hydrolysis in bicarbonate buffered solutions (pH 9.2) at 37 °C; (c) Dissolution rates of Si NMs with different sizes in sodium carbonate, sodium phosphate, sodium chloride, combination of sodium chloride and sodium phosphate buffered solution; (d) Effects of anions on dissolution

rates of Si NMs with the same sodium ion concentration; (e) Effects of cations on dissolution rates of Si NMs with the same phosphate concentration; (f) Effects of cations on dissolution rates of Si NMs with the same chloride concentration; (g) Optical images of an intact Si pad (1000 × 1000 μm) and AFM images of different color area after 4 hours of immersion in the buffer solutions (Na_2HPO_4/NaH_2PO_4 10 mM). KPO and NaPO stands for KH_2PO_4/K_2HPO_4 and NaH_2PO_4/Na_2HPO_4 (molar ratio 19/81), respectively. Solid lines indicate the dissolution behavior by modeling.

Figure 2a, 2b and 2c present the influence of stirring (600 rpm) on the dissolution rates in NaCl (100 mM), Na_2HPO_4/NaH_2PO_4 (10 mM) and K_2HPO_4/KH_2PO_4 (10 mM) solutions with pH 7.4 at 37 °C. Interestingly, a significant decrease of the dissolution rates appears and the size-dependence of dissolution rates disappears under stirring conditions in NaCl, Na_2HPO_4/NaH_2PO_4 and K_2HPO_4/KH_2PO_4 solutions. This behavior is not expected as stirring usually accelerates the dissipation of dissolution products and speeds up dissolution. As shown in Figure S3, the thicknesses remain almost unchanged as a function of time in NaCl, Na_2HPO_4/NaH_2PO_4 and K_2HPO_4/KH_2PO_4 solutions under stirring conditions. Stirring yields dissolution rates of 0.02 ± 0.01 nm/h for all the sizes of Si NMs in both NaCl, Na_2HPO_4/NaH_2PO_4 and K_2HPO_4/KH_2PO_4 solutions. We speculate that such stirring-induced reduction in dissolution rates can be possibly attributed to the interruption of the local enrichment of ions at the Si/solution interface (e.g., physical adsorption), which could have a significant influence on the dissolution rates. Such enrichment of ions could also address the size-dependent behavior, as Si NM with smaller size is more susceptible to the perturbation in the aqueous environments, and therefore slower dissolution

rates have been observed. To further reveal the stirring effects, Figure 2d shows the influence of stirring rates on the dissolution rates of Si NMs. Similarly, the results also show that a significant decrease of the dissolution rates appears and the size-dependence of dissolution rates disappears under low-speed stirring (137 rpm) conditions in Na_2HPO_4/NaH_2PO_4 (10 mM) solutions, indicating stirring introduces reduction in dissolution rates of Si NMs and no obvious difference is observed for different stirring rates (600 rpm and 137 rpm).

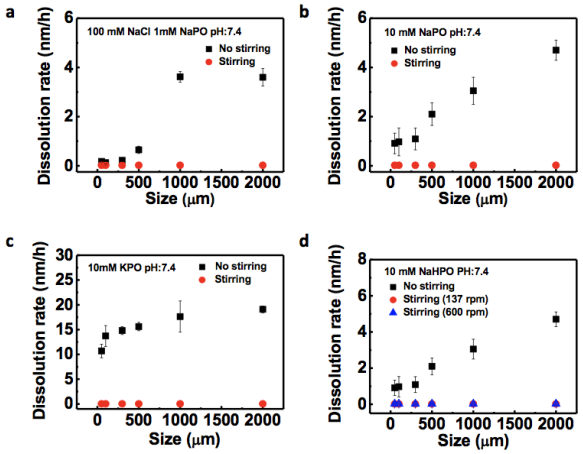

Figure 2. Effects of stirring on the dissolution rates of Si NMs with different sizes in buffer solutions (pH 7.4) at 37 °C. (a) Sodium chloride solution with or without stirring (600 rpm); (b) Sodium phosphate buffered solution with or without stirring (600 rpm); (c) Potassium phosphate solution with or without stirring (600 rpm); (d) Effect of stirring rates on the dissolution rates in sodium phosphate solutions.

The type of dopants and its concentration in Si NMs could possibly modify Si surface charge status and modulate ion adsorption in the solution, thus the influence of dopants on hydrolysis of Si NMs is also systematically investigated to verify the aforementioned hypothesis. The dissolution rates

of Si NMs (2 μm) doped with boron (p type) at three different concentrations (10–20 Ω.cm (10^{15} cm^{-3}), 0.005-0.01 Ω.cm (10^{18} cm^{-3}), <0.0008 Ω.cm (10^{20} cm^{-3})) are studied in both potassium phosphate buffered solutions (K_2HPO_4/KH_2PO_4, 10 mM)) and sodium phosphate buffered solutions (Na_2HPO_4/NaH_2PO_4, 10 mM) at pH 7.4 and 37 °C, and the results appear in Figure 3a-d and Figure S4. Similarly, the rates of Si NMs show the same size-dependent dissolution behavior in all cases and dissolution rates are higher for Si NMs with larger sizes. The results also suggest a strong reduction of dissolution rates with the increase in dopant concentration in both K_2HPO_4/KH_2PO_4 and Na_2HPO_4/NaH_2PO_4 solutions probably due to the decrease of available electrons in the conduction band for hydrolysis, [27] which is consistent with the previously reported results. [17] In addition, relatively lower dissolution rates for all sizes of Si NMs in Na_2HPO_4/NaH_2PO_4 solutions are apparently observed when compared with that in K_2HPO_4/KH_2PO_4 solutions, consistent with the prior results shown in Figure 1e, f. Interestingly, for n-type Si NMs (phosphorus doped, 0.01–0.05 Ω.cm (10^{18} cm^{-3})), size-dependent behavior disappears and similar dissolution rates of Si NMs with different sizes are observed in both K_2HPO_4/KH_2PO_4 solutions (10 mM) and Na_2HPO_4/NaH_2PO_4 solutions (10 mM) with pH 7.4 at 37 °C, as presented in Figure 3e and Figure S5. Similarly, the dissolution rates are higher in K_2HPO_4/KH_2PO_4 solutions than those in Na_2HPO_4/NaH_2PO_4 solutions with the same concentration of phosphates. When the dopant concentration increased to 10^{20} cm^{-3} for n-type Si, a strong reduction of dissolution rate is observed in both potassium phosphate and sodium phosphate solutions, as shown in Figure 3g, which is consistent with the previous reported results. [17] In contrast to p-type Si NMs, stirring (600 rpm) yields twice of the dissolution rates compared to those in non-stirring conditions for n-type Si NMs (buffer solutions with 100 mM NaCl and 10 mM Na_2HPO_4/NaH_2PO_4), as shown in Figure 3f and Figure S5. The solid lines in Figure 3a-d

represent the modeled size-dependent dissolution rates. Table S2 summarize the fitted pre-exponential factor (r_0), the coefficients of size-dependent behavior (b) and the degree of size-dependent dissolution rates of dR/dx.

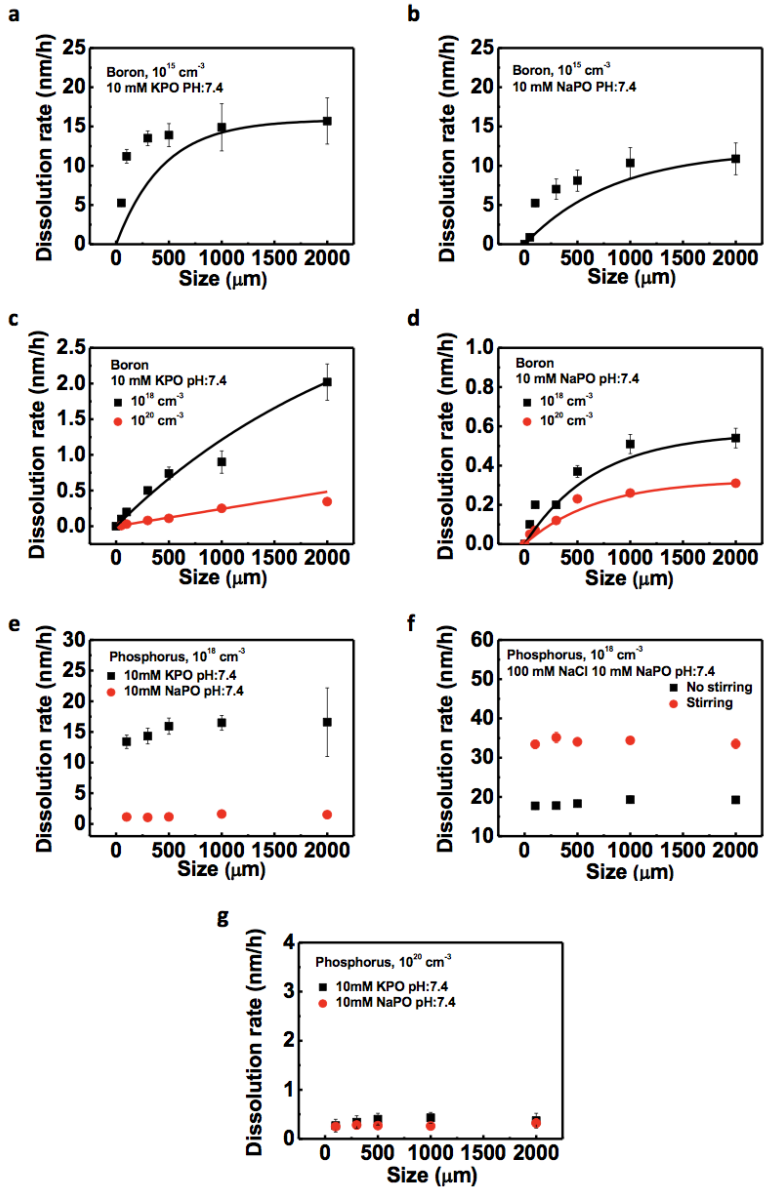

Figure 3. Effects of concentrations and types of dopants on hydrolysis of Si NMs in various types of buffer solutions. (a) Dissolution rates of p-type Si (boron, 10^{15} cm^{-3}) in potassium phosphate buffered solutions; (b) Dissolution rates of p-type Si (boron, 10^{15} cm^{-3}) in sodium

phosphate buffered solutions; (c) Dissolution rates of p-type Si (boron, 10^{18} cm^{-3} and 10^{20} cm^{-3}) in potassium phosphate buffered solutions; (d) Dissolution rates of p-type Si (boron, 10^{18} cm^{-3} and 10^{20} cm^{-3}) in sodium phosphate buffered solutions; (e) Effects of cations on dissolution rates of n-type silicon (phosphorus, 10^{18} cm^{-3}) with different sizes in buffer solutions with the same phosphate concentration; (f) Effect of stirring (600 rpm) on dissolution rates of n-type silicon with different sizes in buffer solution; (g) Dissolution rates of n-type Si (phosphorus, 10^{20} cm^{-3}) in potassium phosphate and sodium phosphate buffered solutions.

These results suggest that the type of dopants do significantly influence the size-dependent dissolution behavior and how the dissolution behavior responses to stirring conditions, which could possibly be attributed to the change of surface charge. When silicon is immersed in an aqueous electrolyte, the Fermi level is disparate across the interface. Equilibrium of this interface thus necessitates a transfer of electrons from one phase to the other and a band-bending phenomenon ensues within silicon, which is dissimilar between p-type and n-type silicon. [29] For an n-type Si, the electrochemical potential is assumed to be more negative than that of the electrolyte. Therefore, after in contact with the solutions, charge will flow from the n-type Si with a more negative initial electrochemical potential to the electrolyte with a more positive electrochemical potential. This interfacial charge-transfer process yields an excess of positive charges on the n-type Si surface and an excess of negative charges on the electrolyte side. By contrast, when a p-type silicon is in contact with the electrolyte, the charge-transfer process results in an excess of negative charges on the p-type silicon surface and an excess of positive charges on the electrolyte side. [30] To verify the difference, the surface zeta potential of p-type and n-type Si in saline buffered solutions with pH 7.4 are measured using SurPASS solid samples zeta potential

analyzer (Anton-Paar, Austria), and the results are summarized in Table 1 and Table S3. Although the surface zeta potential of p-type Si strongly varies in various saline buffered solutions, they are all negative, suggesting the accumulation of electrons on the surface of p-type Si. In contrast with p-type Si, the surface zeta potential value of n-type Si is positive, indicating positive charges on the surface of n-type Si as a consequence of equilibrium with the Fermi level. It is noted that due to the relatively large deviation of the surface zeta potential measurement, the results are for qualitative comparison. In all, the change of surface charge status of Si could possibly influence the ion adsorption behavior at the Si/solution interface, and therefore gives rise to the size-dependent hydrolysis behavior and stirring-induced reduction in dissolution rates. These results shed light on new methods to modulate the lifetime of Si NMs for associated biodegradable electronics.

Table 1. Zeta potential of p-type and n-type silicon in various types of buffer solutions (pH 7.4) at room temperature.

Solution	**Si sample**	**ZP(HS) (mV)**
NaCl (100 mM)	p type	-75.42±70.24
KCl (100 mM)	p type	-15.95±6.13
NaPO (10 mM)	p type	-111.4±70.24
NaPO (10 mM)	n type	17.83±15.44

To understand the ion distribution near the Si surface, we further performed molecular dynamics (MD) simulations. Figure 4a depicts the atomistic modeling composed of Si NMs (100) in the water solution of 0.4 M sodium phosphate and 0.4 M sodium chloride with pH 7.4. Figure 4b shows the number density profile of Na^+ near the silicon surface with different charge densities. The strong fluctuation with a peak close to the silicon surface indicates an obvious enrichment of ions. The enrichment becomes stronger at a negatively charged surface in comparison with a positively charged one due to the enhanced electrostatic interactions with Na^+ and will increase with the increasing of charge density. When the distance is far away from the silicon surface, the effect of surface charge will be approximately the same due to the fast decay of confined solid-liquid interfacial interaction. Similar results are also obtained in the number density profile of phosphate anions (including both $H_2PO_4^-$ and HPO_4^{2-}), as shown in Figure 4c, and the number density increases as the surface charge becomes more negative. By contrast, the density of Cl^- shows insignificant change with the varied polarity and density of surface charge, indicating less enrichment at the Si/solution interface (Figure 4d). Besides, the negatively charged surface suppresses the absorption of Cl^- due to the repulsive electrostatic interaction. The different absorption behavior of Cl^- and phosphates at the charged surface results from their interaction with Na^+, as indicated by the radical distribution functions (RDF) of Na^+/ phosphate and Cl^-/phosphate in Figure 4e. The analysis on RDF shows that the first solvation shell of Na^+/ phosphate and Cl^- /phosphate is 0.41 nm and 0.57 nm, respectively, and a smaller equilibrium distance of atom pairs between Na^+ and phosphates indicates a stronger interaction. These results suggest that Na^+ prefer to be absorbed on Si surface through electrostatic interaction, while phosphates are closely interacted with Na^+ over that of Cl^-. More negatively charged surface results in higher enrichment of Na^+ and phosphates, consistent with the aforementioned hypothesis that different Si charge

status will influence the ion distribution at the Si/solution interface. Due to the stronger interaction with Na^+/phosphates compared to that of Cl^-/phosphates, phosphates stay closer to the Si surface, which corresponds to the higher enhanced dissolution rates through nucleophilic attack in the presence of phosphates, as shown in the experimental data. When the concentration of sodium phosphates in the buffer solutions decreases, further simulations (Figure S6 a-d) shows a weaker Na^+/phosphates interaction and therefore leading to a slower dissolution rate with a weaker size-dependent effect, also consistent with the experimental data.

Besides, when the solution of sodium phosphate and sodium chloride changes to that of potassium phosphate and potassium chloride with the same concentration and pH level, our simulations show a stronger interaction of K^+ ions with silicon surface than that of Na^+ ions, as evidenced by a large peak number density of K^+ ions in Figure 4f and Figure S7 a-c. This strong interaction also agrees well with a higher frequency of solvent exchange rate k_{ex} (s^{-1}) of K^+ (Na^+ and K^+ is $10^{9.0}$ and $10^{9.2}$, respectively [31]) that reflects the exchange of primary solvation waters associated with individual cations with the surrounding aqueous environment (e.g. anions), suggesting that more anions could be accessible at the Si/solution interface to assist dissolution. This is consistent with the higher dissolution rates of Si NMs in the potassium solution environment observed in experiments.

With these simulation and experimental results, the underlying mechanisms of hydrolysis behavior is believed to be significantly different for p-type and n-type Si NMs that possess different surface charge statuses, and is schematically illustrated in Figure 4g. For p-type silicon associated with a negatively charged surface, the Na^+ adsorption occurs on the silicon surface owing to the

electrostatic interactions between cations (Na^+) and negative charges. The enrichment of group IA cations (Na^+ and K^+) could accelerate Si dissolution because of their potential ability to deprotonate surface silanol groups and/or to enhance the reactivity of water and siloxane groups, similar to that of group IIA cations (Ca^{2+} and Mg^{2+}) as suggested in the previous reports for Si and SiO_2 dissolution studies. [22, 32] As a consequence of Na^+ enrichment, an increase of density of phosphates also occurs at the surface due to the strong electrostatic interaction between anions (phosphates) and cations (Na^+), leading to the enrichment of phosphates at the Si/solution interface. The enrichment of phosphates can interact with the silicon surface through nucleophilic attack to weaken the interior bonds of silicon surface atoms, and further assist in silicon dissolution, as shown in Figure 4h, also reported in a previous paper. [26] On the contrary, the level of enrichment of chlorides at the interface is relatively lower and less sensitive to surface charge density (Figure 4d), which could account for the lower dissolution rates of Si NMs in chloride solutions compared to that in phosphate solutions with the same amount of Na^+ (Figure 1d). Moreover, the enrichment of ions is sensitive to perturbation, e.g. stirring, random thermal agitation, fluid movement, etc., therefore leading to local non-uniform (location-dependent) dissolution behavior as shown previously in Figure 1b, 1g and S1. Si NMs with smaller size are more susceptible to disturbance, and therefore size-dependent dissolution rates are observed. Stirring could significantly interrupt the surface enrichment, and therefor disappearance of size-dependent behavior as well as significant reduction of dissolution rates have been observed (Figure 2). By contrast, the concentrations of adsorptive Na^+ and phosphates on the surface of n-type silicon are relatively lower (less enrichment), therefore the dissolution rates of n-type Si NMs with different sizes show no apparent difference in both K_2HPO_4/KH_2PO_4 solutions and Na_2HPO_4/NaH_2PO_4 solutions, and

stirring can speed up the dissolution as it removes the dissolution products and drives the reaction moving forward.

In addition, to show a quantitative relationship between ion enrichment and surface charge density, the number densities of phosphates, sodium and chloride ions at their first peaks that are closest to the substrate in their distribution at different surface charge densities are compared, as shown in Figure S7d. As surface charge density varies from negative to positive, the peak density of sodium ions and phosphates decrease significantly, indicating a weakened enrichment. Besides, the consistency of their decreasing trends verifies the strong interaction between sodium ions and phosphates. In contrary, the peak density of chloride ions increases slightly, suggesting an enhanced enrichment effect to some extent.

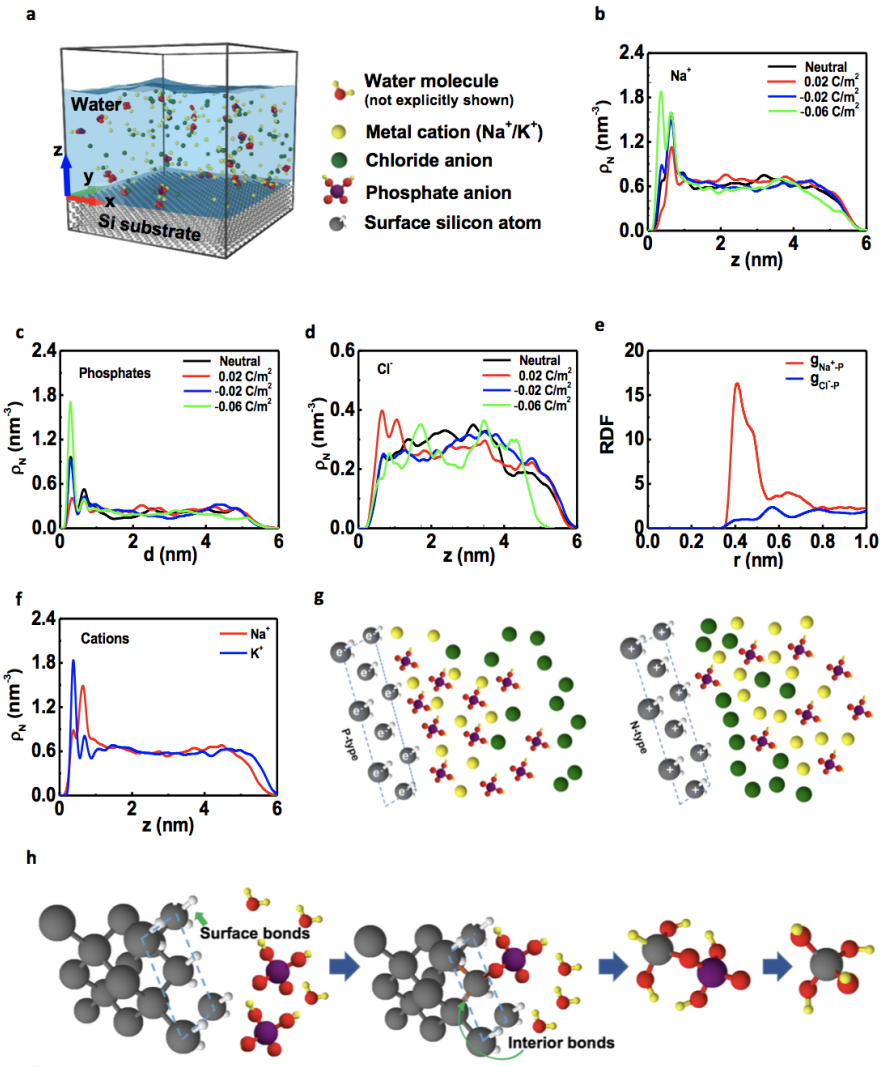

Figure 4. Molecular dynamics (MD) simulations of liquid-solid interactions and schematic mechanism of silicon dissolution. (a) Atomistic modeling of the buffer solution in the contact of Si {100} surface; Number density of (b) sodium ion (Na^+), (c) phosphate, and (d) chloride ion (Cl^-) with respect to the silicon surface with various charge surface densities. The buffer solution contains 0.4 M NaCl and 0.4 M phosphates; (e) The radial density function (RDF) of Na^+/phosphate and Cl^-/phosphate. The buffer solution contains 0.4 M NaCl and 0.4 M phosphates and the surface charge density is -0.02 C/m^2; (f) Comparison of number density of sodium (Na^+) and potassium(K^+) ions near the silicon surface. The buffer solution contains 0.4

M NaCl and 0.4 M phosphates and the surface charge density is -0.02 C/m^2; (g) Schematic illustrations of atomic configuration of each ion adsorption event for p-type (left) and n-type (right) silicon; (h) Process of hydrolysis of Si.

Measurements of the enrichment of chlorides at Si surface has been attempted by an XMU-BY-1 scanning electrochemical workstation system (Xiamen university, China) in NaCl (500 mM) solutions with pH 7.4 at room temperature. Figure 5a shows the dissolution rates of Si NMs (p typed (boron), 10^{17} cm^{-3}, (100), 200 nm) with different size in NaCl solutions (500 mM pH 7.4) at room temperature. Figure S3c presents the change in thickness as a function of time. Similarly, the dissolution rates of Si NMs with a larger size is higher than that with a smaller size. Figure S3f highlights the color change of Si NMs with different sizes after immersion in NaCl (500 mM) solution for 6 hours. The results show that the dissolution of Si NMs is spatially nonuniform. Figure 5b and c presents the concentration measurements on patterned Si squares as a function of different sizes after immersion in NaCl (500 mM) solution for 6 hours. Figure 5b gives the average concentration of Cl^- over an entire Si square, while Figure 5c gives the concentration measured at a certain point over a Si square. Both results show that the concentration of Cl^- enhances slightly with the increase in the size of Si NMs. Figure 5d shows the mapping of Cl^- concentration over Si squares with different sizes (2000 × 2000 μm, 1000 × 1000 μm, 500 × 500 μm) with the scanning area of 1000 × 1000 μm, 1000 × 1000 μm, 3000 × 3000 μm, respectively, after soaking in 500 mM NaCl solution for 2 hours (the value on the scale bar illustrates the relative concentration of chlorides), wherein the relatively lighter color intensity represents a higher concentration of Cl^-. It shows apparently adsorption of Cl^- for larger Si pad (2000 × 2000 μm), while the adsorption effects significantly decrease with the reduction of Si size. Nevertheless, the measured level of enrichment

of chlorides on the surface is relatively low, consistent with the simulation results shown before. Due to the limited space of the sample platform (Φ 3 × 5 cm) of the XMU-BY-1 scanning electrochemical workstation system, introducing mechanical stirring is impeded. Future improvements of the system could allow further detailed studies of more versatile ion concentration mapping and the influence of stirring conditions.

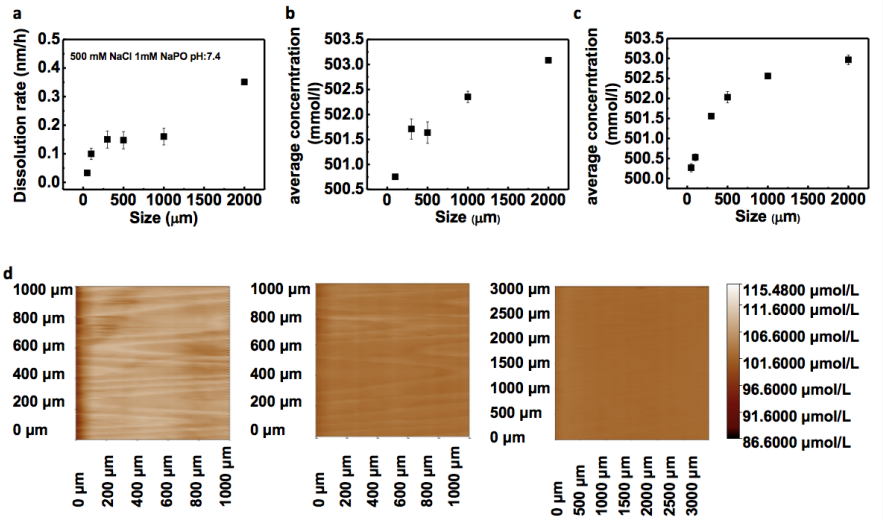

Figure 5. Dissolution of Si NMs in 500 mM NaCl buffer solution (pH 7.4) at room temperature. (a) Dissolution rates of Si NMs with different sizes; (b) The average concentration of chloride ions on the surface of Si pad after 6 hours immersion; (c) The average concentration of chloride ions on the surface of a certain point of Si pad after 6 hours immersion; (d) Concentration distribution of Si pads (2000 × 2000 μm, 1000 × 1000 μm, 500 × 500 μm) with the scanning area of 1000 × 1000 μm, 1000 × 1000 μm, 3000 × 3000 μm, respectively, after 2 hours immersion (the value on the scale bar illustrates relatively concentration of the chlorides).

These experimental and computational studies reveal new methods to modulate the dissolution rates of Si NMs, suggesting changing the surface charge status can influence the distribution of ions at the Si/solution and therefore resulting in size-dependent hydrolysis and stirring-induced reduction in dissolution rates. The arrays of Si membranes can potentially be used as passive bioresorbable electrodes on the cerebral cortex to record electrocorticography (ECoG) signals and somatosensory-evoked potentials (EPs), [7] or as the encapsulation layer for bioresorbable ECoG metallic electrodes. [22] Precise and versatile modulation of operational lifetime of Si membranes to satisfy practical applications remains as one key challenge for these applications, e.g., adequately location of seizures for epilepsy surgery can take for 1-3 months. Here, utilizing the size-dependent behavior, we demonstrate a strategy to modulate the lifetime of Si recording electrodes based on Si NMs through geometry design as an example, and the results appear in Figure 6. Two types of structures for the electrodes are designed, pad-type and mesh-type, with the overall area of 300 × 300 μm. Figure 6a, b presents the optical images of Si recording electrodes, and the Si sensing pads at different stages of hydrolysis in buffer solutions (100 mM NaCl and 10 mM Na_2HPO_4/NaH_2PO_4, pH 7.4) at 37 °C. Figure 6c and 6d presents the SEM image of Si pad-type and mesh-type electrode under pristine state and final state, the results show that the surface of Si electrodes become rougher as dissolution proceeds and a non-uniform dissolution behavior can be observed. Figure 6e shows the change in thickness as a function of time. The results show that the pad-type electrode dissolved nearly four times faster compared to that of the mesh-type electrode, in the sense that the rate of dissolution of the Si pad is ~0.56 nm/h, while the dissolution rate of mesh Si is ~0.12 nm/h. The electrochemical impedance spectra (EIS) of both pad-type and mesh-type Si electrodes are evaluated in aqueous buffer solutions (100 mM NaCl and 10 mM Na_2HPO_4/NaH_2PO_4, pH 7.4) at room temperature (Figure 6f), and the results show that the

magnitude for pad-type and mesh-type Si electrodes is 682 and 2006 Ω, respectively, at frequencies most relevant for neural sensing (near 1 KHz). These results suggest a tunable operational lifetime of Si recording electrodes can be achieved by simple geometry design, providing a new alternative strategy to control the degradability of biodegradable electronics.

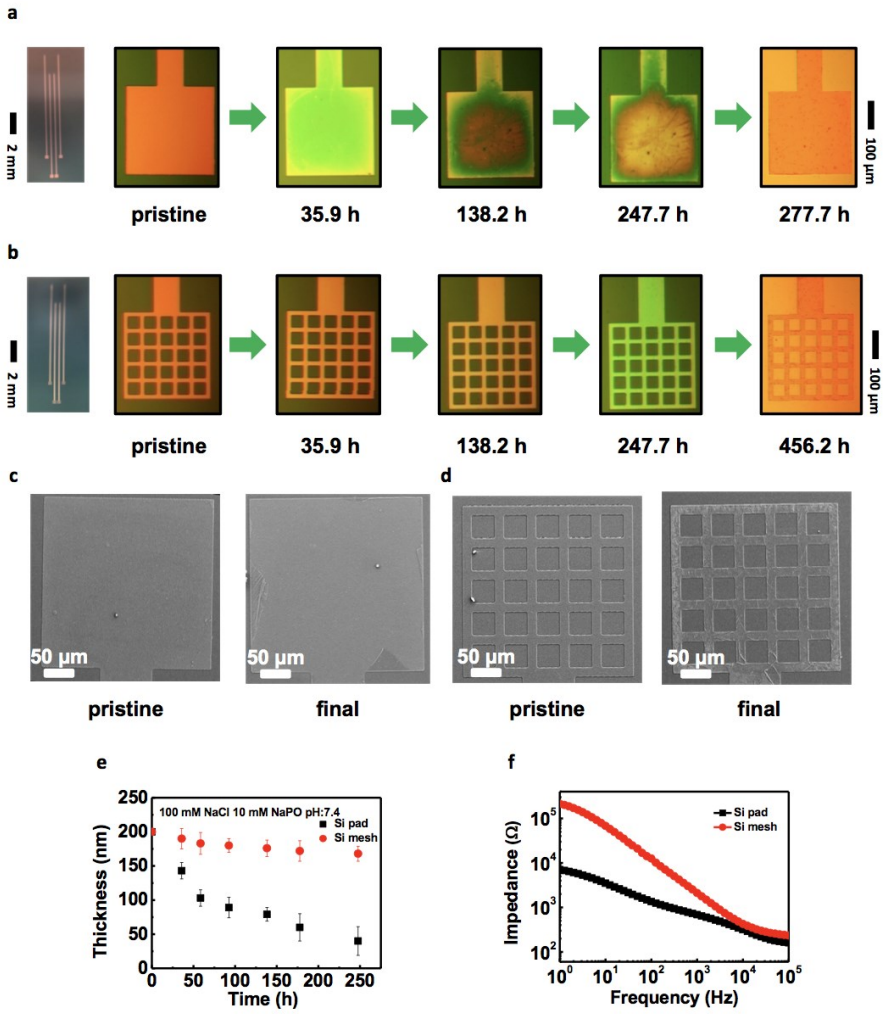

Figure 6. Si electrode arrays based on Si NMs. (a) Optical images of the dissolution process of Si pad-type electrode; (b) Optical images of the dissolution process of Si mesh-type electrode; (c) SEM image of Si pad-type electrode under pristine state and final state; (d) SEM image of Si mesh-type electrode under pristine state and final state; (e) Change in thickness of Si pad and Si

mesh as a function of time; (f) Electrochemical impedance spectrum of four electrodes for Si pad and Si mesh.

Conclusions

New mechanism of the hydrolysis of Si NMs is revealed through systematic studies in the current work. Dissolution behavior is significantly influenced by the surface charge status of Si NMs, which can modify the ion adsorptions at the Si/solution interface and give rise to unusual size-dependent hydrolysis and stirring-induced reduction in dissolution rates. The dissolution rates of Si NMs are also accelerated in the presence of phosphates and potassium ions, and are decelerated with higher dopant levels. Molecular dynamics (MD) simulations are performed to probe the underlying mechanism by investigating the ion distribution near charged silicon surface and show qualitative agreement with experimental observations. Tunable lifetime of recording arrays based on Si NMs is achieved through geometrical design. These results shed light on new strategies to control the operational time frames of Si NMs for biodegradable electronics, through charge carrier modulation, geometrical design, surface chemistry modification, etc. Additional possibilities include introducing triggered degradation mechanism to build smart biodegradable electronics with on-demand capability. As Si is a critical constituent component for high-performance biodegradable electronics that ensures sophisticated functionality at system levels, this work provides an important fundamental understanding to modulate materials degradation through versatile strategies and will further expand opportunities for applications in electronic biomedicine.

Experimental Methods

Fabrication of Si NMs and Dissolution Experiments

Fabrication of arrays of Si NMs began with silicon-on-insulator (SOI) wafers with a top silicon layer. Si NMs (100 direction) here are doped with boron (10^{15} cm^{-3}, 10^{18} cm^{-3}, 10^{20} cm^{-3}) or phosphorus (10^{18} cm^{-3}) with 200 nm and 2 μm thickness. The top Si on the SOI wafer was then patterned into arrays of squares with different size (2000 × 2000 μm, 1000 × 1000 μm, 500 × 500 μm, 300 × 300 μm, 100 × 100 μm, 50 × 50 μm) by photolithography and reactive ion etching (RIE) with sulfur hexafluoride gas (SF_6). Phosphate buffered solutions with different concentrations at pH 7.4 were prepared by sodium/potassium monobasic and dibasic (molar ratio 19.8/80.2). Buffered chloride solutions were prepared by adding 1 mM phosphate buffered solutions to chloride solutions to maintain a constant pH. To eliminate the native oxide of Si NMs, sample surface was treated with a buffered oxide etchant (BOE, 6:1) for a few seconds before dissolution experiments. The dissolution experiments were performed by immersing the samples into aqueous buffer solutions, extracting them after a certain time, measuring the thickness by profilometry, and then re-immersing the samples into the solutions. The buffer solutions were replaced every day to maintain a constant concentration throughout the test. Each reported thickness data as a function of time corresponding to an average of at least 10 measurements, and the error bars represent the standard deviation of the data. Linear fitting of the average thickness at times determined the dissolution rates of Si NMs, and the error bars represent the error in slope of linear fitting.

Molecular Dynamics (MD) Simulation and Method

All the molecular dynamics simulations were performed with LAMMPS. [33] The time step was set as 0.5 fs. To model the system of Si/solution interface, a revised AMBER potential was applied to describe the intramolecular behavior of phosphate anions, [34] the most popular SPC/E model was applied to simulate water molecules. [35] The interactions between molecules were described by 12-6 Lennard-Jones interaction along with the Lorentz–Berthelot mixing rule, [36] as well as the long-range Coulomb interaction evaluated by the particle-particle-particle-mesh (PPPM) with a root mean of 0.0001. The dimension of Si substrate was 9.18 nm × 9.56 nm × 1.50 nm, and the plane {100} was set in contact with solution molecules. To model the effect of surface charge, for simplification, an extra charge was uniformly distributed to each Si atom of surface. The initial number ratio of phosphate ions ($H_2PO_4^-$/HPO_4^{2-}) was determined by their ionization constants with pH=7.4 at 300 K [37] and it was 0.6754 in the modeling. The substrate was fixed during simulation process. Periodic boundary condition was applied in the directions parallel to the Si/solution interface and non-periodic boundary condition was applied in the direction perpendicular to the Si/solution interface. In the simulations, the system was first equilibrated to achieve a full mixture of the solution at 300K and 1 atm. in NVT ensemble for 5 ns and then microcanonical (NVE) ensemble was employed to study the coordination and interaction of solid and liquid.

Concentration Distribution Measurement

The concentration distribution of Cl^- on silicon surface in NaCl (500 mM) solutions was measured with an XMU-BY-1 scanning electrochemical workstation system (Xiamen University, China). This system consists of scanning tunneling microscope mode and scanning reference electrode technique mode. In the scanning reference electrode mode, micro-reference probes are platinum

(Pt) electrode for reference electrode and silver/silver chloride electrode (Ag/AgCl, Φ 20 μm) for working electrode due to its sensitivity to concentrations of Cl^-. The distance between the scanning micro-reference probe tip and the specimen surface (50 μm) was controlled accurately by a high-resolution piezoelectric stack/tube in the scanning tunneling microscope mode. The average concentration of Cl^- on silicon pad surface (512 × 512 points) and a certain point of silicon pad surface was measured for about 6 hours.

AFM measurements

The roughness of Si NMs after 4 hours of immersion in phosphate buffered solutions (Na_2HPO_4/NaH_2PO_4 10 mM) is measured by atomic force microscopy (AFM, Bruker Multimode 8) with a peak-force tapping mode and an amplitude set point of 364 mV.

Zeta potential measurement

The surface zeta potential of Si NMs in saline buffered solutions (pH 7.4) at room temperature were measured by SurPASS solid samples zeta potential analyzer (Anton-Paar, Austria), which includes an analyzer, a data control system, and an adjustable gap cell. Two Si samples (20 × 10 mm) were fixed on sample holders using double-sided adhesive tape. The distance between the sample surfaces was adjusted to be ~100 μm. Three kinds of electrolyte solutions including NaCl (100 mM), KCl (100 mM) and Na_2HPO_4/NaH_2PO_4 (10 mM) with a target ramp pressure of 300 mbar were used in the measurements.

EIS measurement

Electrochemical impedance spectra (EIS) of the Si recording electrodes were measured by a Gamry Interface 1000E Potentiostat in buffer solutions (100 mM NaCl and 10 mM Na_2HPO_4/NaH_2PO_4, pH 7.4) at room temperature through a three-electrode configuration, with Si recording electrodes as the working electrode, Ag/AgCl as the reference electrode, and Pt as the counter electrode. The EIS was obtained by varying frequency over a range (1 Hz – 1 MHz) relevant for neural sensing, via application of a sinusoidal AC excitation signal (5 mV amplitude, 0 V bias from the open circuit voltage).

Optical microscope observation

An optical microscope (Phenix, China) was used to examine the surface morphologies of Si NMs at various stages of dissolution in buffer solutions (Na_2HPO_4/NaH_2PO_4 10 mM at 37 °C and NaCl 500 mM at room temperature, respectively), using the magnification of 50 ×.

Supporting Information.

Figures that summarize change in thickness of Si NMs with different doping levels as a function of time in various types of saline buffered solutions with molar concentrations and pHs close to physiological condition at 37 °C; Effects of stirring on the hydrolysis of Si NMs in different types of buffer solutions at 37 °C and dissolution of Si NMs in 500 mM NaCl (pH 7.4) at room temperature; MD simulations on the effects of concentration of the buffer solutions and the effects of different buffer solutions; Values of r_0, coefficient of size-dependent effect (b) and

d*R*/d*x* of Si NMs in various types of buffer solutions; Zeta potential of p-type and n-type silicon in various types of buffer solutions (pH 7.4) at room temperature. (PDF)

Corresponding Author

*Corresponding authors: lanyin@tsinghua.edu.cn; bx4c@virginia.edu.

Author Contributions

The manuscript was written through contributions of all authors. All authors have given approval to the final version of the manuscript. ♦Liu Wang and Yuan Gao contributed equally to this work.

Acknowledgments

This work was supported by National Natural Science Foundation of China (NSFC) 51601103 (L.Y.), 1000 Youth Talents Program in China (L.Y.) and China Postdoctoral Science Foundation 2018M641341 (L. W.). B.X. acknowledges the start-up funds at the University of Virginia and NSF-CBET-1805451. X. Sheng acknowledges support from National Natural Science Foundation of China (grant No. 51602172).

References

1. Hwang, S.-W.; Tao, H.; Kim, D.-H.; Cheng, H.; Song, J.-K.; Rill, E.; Brenckle, M. A.; Panilaitis, B.; Won, S. M.; Kim, Y.-S.; Song, Y. M.; Yu, K. J.; Ameen, A.; Li, R.; Su, Y.; Yang, M.; Kaplan, D. L.; Zakin, M. R.; Slepian, M. J.; Huang, Y.; Omenetto, F. G.; Rogers, J. A., A Physically Transient Form of Silicon Electronics. *Science* **2012,** *337* (6102), 1640-1644.

2. Hwang, S. W.; Park, G.; Cheng, H.; Song, J. K.; Kang, S. K.; Yin, L.; Kim, J. H.; Omenetto, F. G.; Huang, Y.; Lee, K. M., 25th Anniversary Article: Materials for High-performance Biodegradable Semiconductor Devices. *Advanced Materials* **2014,** *26* (13), 1992-2000.

3. Kim, D.-H.; Kim, Y.-S.; Amsden, J.; Panilaitis, B.; Kaplan, D. L.; Omenetto, F. G.; Zakin, M. R.; Rogers, J. A., Silicon Electronics on Silk as a Path to Bioresorbable, Implantable Devices. *Applied Physics Letters* **2009,** *95* (13), 133701.

4. Irimia-Vladu, M., "Green" Electronics: Biodegradable and Biocompatible Materials and Devices for Sustainable Future. *Chem. Soc. Rev.* **2014,** *43* (2), 588-610.

5. Hwang, S. W.; Huang, X.; Seo, J. H.; Song, J. K.; Kim, S.; Hage-Ali, S.; Chung, H. J.; Tao, H.; Omenetto, F. G.; Ma, Z., Materials for Bioresorbable Radio Frequency Electronics. *Advanced Materials* **2013,** *25* (26), 3526-3531.

6. Kang, S.-K.; Murphy, R. K.; Hwang, S.-W.; Lee, S. M.; Harburg, D. V.; Krueger, N. A.; Shin, J.; Gamble, P.; Cheng, H.; Yu, S., Bioresorbable Silicon Electronic Sensors for the Brain. *Nature* **2016,** *530* (7588), 71-76.

7. Yu, K. J.; Kuzum, D.; Hwang, S.-W.; Kim, B. H.; Juul, H.; Kim, N. H.; Won, S. M.; Chiang, K.; Trumpis, M.; Richardson, A. G., Bioresorbable Silicon Electronics for Transient Spatiotemporal Mapping of Electrical Activity from the Cerebral Cortex. *Nature materials* **2016,** *15* (7), 782-791.

8. Lu, L.; Yang, Z.; Meacham, K.; Cvetkovic, C.; Corbin, E. A.; Vázquez-Guardado, A.; Xue, M.; Yin, L.; Boroumand, J.; Pakeltis, G., Biodegradable Monocrystalline Silicon Photovoltaic Microcells as Power Supplies for Transient Biomedical Implants. *Advanced Energy Materials* **2018**, 1703035.

9. Yin, L.; Cheng, H.; Mao, S.; Haasch, R.; Liu, Y.; Xie, X.; Hwang, S. W.; Jain, H.; Kang, S. K.; Su, Y., Dissolvable Metals for Transient Electronics. *Advanced Functional Materials* **2014,** *24* (5), 645-658.

10. Yin, L.; Huang, X.; Xu, H.; Zhang, Y.; Lam, J.; Cheng, J.; Rogers, J. A., Materials, Designs,

and Operational Characteristics for Fully Biodegradable Primary Batteries. *Advanced Materials* **2014,** *26* (23), 3879-3884.

11. Jia, X.; Wang, C.; Ranganathan, V.; Napier, B.; Yu, C.; Chao, Y.; Forsyth, M.; Omenetto, F. G.; MacFarlane, D. R.; Wallace, G. G., A Biodegradable Thin-Film Magnesium Primary Battery Using Silk Fibroin–Ionic Liquid Polymer Electrolyte. *ACS Energy Letters* **2017,** *2* (4), 831-836.

12. Tsang, M.; Armutlulu, A.; Martinez, A. W.; Allen, S. A. B.; Allen, M. G., Biodegradable Magnesium/Iron Batteries with Polycaprolactone Encapsulation: A Microfabricated Power Source for Transient Implantable Devices. *Microsystems & Nanoengineering* **2015,** *1*, 15024.

13. Kang, S. K.; Hwang, S. W.; Cheng, H.; Yu, S.; Kim, B. H.; Kim, J. H.; Huang, Y.; Rogers, J. A., Dissolution Behaviors and Applications of Silicon Oxides and Nitrides in Transient Electronics. *Advanced Functional Materials* **2014,** *24* (28), 4427-4434.

14. Kang, S. K.; Hwang, S. W.; Yu, S.; Seo, J. H.; Corbin, E. A.; Shin, J.; Wie, D. S.; Bashir, R.; Ma, Z.; Rogers, J. A., Biodegradable Thin Metal Foils and Spin-On Glass Materials for Transient Electronics. *Advanced Functional Materials* **2015,** *25* (12), 1789-1797.

15. Hwang, S. W.; Song, J. K.; Huang, X.; Cheng, H.; Kang, S. K.; Kim, B. H.; Kim, J. H.; Yu, S.; Huang, Y.; Rogers, J. A., High-Performance Biodegradable/Transient Electronics on Biodegradable Polymers. *Advanced Materials* **2014,** *26* (23), 3905-3911.

16. Feig, V. R.; Tran, H.; Bao, Z., Biodegradable Polymeric Materials in Degradable Electronic Devices. *ACS central science* **2018,** *4* (3), 337-348.

17. Hwang, S.-W.; Park, G.; Edwards, C.; Corbin, E. A.; Kang, S.-K.; Cheng, H.; Song, J.-K.; Kim, J.-H.; Yu, S.; Ng, J., Dissolution Chemistry and Biocompatibility of Single-Crystalline Silicon Nanomembranes and Associated Materials for Transient Electronics. *ACS nano* **2014,** *8* (6), 5843-5851.

18. Kang, S.-K.; Park, G.; Kim, K.; Hwang, S.-W.; Cheng, H.; Shin, J.; Chung, S.; Kim, M.; Yin, L.; Lee, J. C., Dissolution Chemistry and Biocompatibility of Silicon- and Germanium- Based Semiconductors for Transient Electronics. *ACS applied materials & interfaces* **2015,** *7* (17), 9297-9305.

19. Dagdeviren, C.; Hwang, S. W.; Su, Y.; Kim, S.; Cheng, H.; Gur, O.; Haney, R.; Omenetto, F. G.; Huang, Y.; Rogers, J. A., Transient, Biocompatible Electronics and Energy Harvesters Based on ZnO. *Small* **2013,** *9* (20), 3398-3404.

20. Chen, X.; Park, Y. J.; Kang, M.; Kang, S.-K.; Koo, J.; Shinde, S. M.; Shin, J.; Jeon, S.; Park, G.; Yan, Y., CVD-Grown Monolayer MoS_2 in Bioabsorbable electronics and Biosensors. *Nature communications* **2018,** *9* (1), 1690.

21. Zhou, W.; Dai, X.; Fu, T.-M.; Xie, C.; Liu, J.; Lieber, C. M., Long Term Stability of Nanowire Nanoelectronics in Physiological Environments. *Nano letters* **2014,** *14* (3), 1614-1619.

22. Lee, Y. K.; Yu, K. J.; Song, E.; Farimani, A. B.; Vitale, F.; Xie, Z.; Yoon, Y.; Kim, Y.; Richardson, A.; Luan, H.; Wu, Y.; Xie, X.; Lucas, T. H.; Crawford, K.; Mei, Y.; Feng, X.; Huang, Y.; Litt, B.; Aluru, N. R.; Yin, L.; Rogers, J. A., Dissolution of Monocrystalline Silicon Nanomembranes and Their Use as Encapsulation Layers and Electrical Interfaces in Water-Soluble Electronics. *Acs Nano* **2017,** *11* (12), 12562-12572.

23. Chang, J.-K.; Fang, H.; Bower, C. A.; Song, E.; Yu, X.; Rogers, J. A., Materials and Processing Approaches for Foundry-Compatible Transient Electronics. *Proceedings of the National Academy of Sciences* **2017,** *114* (28), E5522-E5529.

24. Chang, J. K.; Chang, H. P.; Guo, Q.; Koo, J.; Wu, C. I.; Rogers, J. A., Biodegradable Electronic Systems in 3D, Heterogeneously Integrated Formats. *Advanced Materials* **2018,** *30* (11), 1704955.

25. Yin, L.; Bozler, C.; Harburg, D. V.; Omenetto, F.; Rogers, J. A., Materials and Fabrication Sequences for Water Soluble Silicon Integrated Circuits at the 90 nm Node. *Applied Physics Letters* **2015,** *106* (1), 014105.

26. Yin, L.; Farimani, A. B.; Min, K.; Vishal, N.; Lam, J.; Lee, Y. K.; Aluru, N. R.; Rogers, J. A., Mechanisms for Hydrolysis of Silicon Nanomembranes as Used in Bioresorbable Electronics. *Advanced Materials* **2015,** *27* (11), 1857-1864.

27. Seidel, H.; Csepregi, L.; Heuberger, A.; Baumgärtel, H., Anisotropic Etching of Crystalline Silicon in Alkaline Solutions II. Influence of Dopants. *Journal of the Electrochemical Society* **1990,** *137* (11), 3626-3632.

28. Seidel, H.; Csepregi, L.; Heuberger, A.; Baumgärtel, H., Anisotropic Etching of Crystalline Silicon in Alkaline Solutions I. Orientation Dependence and Behavior of Passivation Layers. *Journal of the electrochemical society* **1990,** *137* (11), 3612-3626.

29. Rajeshwar, K., Fundamentals of Semiconductor Electrochemistry and Photoelectrochemistry. *Encyclopedia of electrochemistry* **2007,** *6*, 1-53.

30. Tan, M. X.; Laibinis, P. E.; Nguyen, S. T.; Kesselman, J. M.; Stanton, C. E.; Lewis, N. S., Principles and Applications of Semiconductor Photoelectrochemistry. *Progress in inorganic chemistry* **1994**, 21-144.

31. Antonini, A. C.; Blandamer, M. J.; Burgess, J.; Hakin, A. W.; Hall, N. D.; Blandamer, A. H., Pairwise Interaction Parameters for Sodium, Potassium and Halide Ions in Aqueous Solutions. *Journal of the Chemical Society, Faraday Transactions 1: Physical Chemistry in Condensed Phases* **1988,** *84* (6), 1889-1896.

32. Dove, P. M.; Nix, C. J., The Influence of the Alkaline Earth Cations, Magnesium, Calcium, and Barium on the Dissolution Kinetics of Quartz. *Geochimica et Cosmochimica Acta* **1997,** *61*

(16), 3329-3340.

33. Plimpton, S., Fast Parallel Algorithms for Short-Range Molecular Dynamics. *Journal of computational physics* **1995,** *117* (1), 1-19.

34. Steinbrecher, T.; Latzer, J.; Case, D., Revised AMBER Parameters for Bioorganic Phosphates. *Journal of chemical theory and computation* **2012,** *8* (11), 4405-4412.

35. Mark, P.; Nilsson, L., Structure and Dynamics of the TIP3P, SPC, and SPC/E Water Models at 298 K. *The Journal of Physical Chemistry A* **2001,** *105* (43), 9954-9960.

36. Zhao, J.; Culligan, P. J.; Qiao, Y.; Zhou, Q.; Li, Y.; Tak, M.; Park, T.; Chen, X., Electrolyte Solution Transport in Electropolar Nanotubes. *Journal of Physics: Condensed Matter* **2010,** *22* (31), 315301.

37. Powell, K. J.; Brown, P. L.; Byrne, R. H.; Gajda, T.; Hefter, G.; Sjöberg, S.; Wanner, H., Chemical Speciation of Environmentally Significant Heavy Metals with Inorganic Ligands. Part 1: The Hg^{2+}–Cl^-, OH^-, CO_3^{2-}, SO_4^{2-}, and PO_4^{3-} Aqueous Systems (IUPAC Technical Report). *Pure and applied chemistry* **2005,** *77* (4), 739-800.

Table of Contents graphic